Article

Recovery of isolated lithium through discharged state calendar ageing

https://doi.org/10.1038/s41586-023-06992-8

Received: 29 March 2023

Accepted: 18 December 2023

Published online: 7 February 2024

Check for updates

Wenbo Zhang[1,5], Philaphon Sayavong[2,5], Xin Xiao[1], Solomon T. Oyakhire[3], Sanzeeda Baig Shuchi[3], Rafael A. Vilá[1], David T. Boyle[2], Sang Cheol Kim[1], Mun Sek Kim[3], Sarah E. Holmes[2], Yusheng Ye[1], Donglin Li[1], Stacey F. Bent[3] & Yi Cui[1,4]✉

Rechargeable Li-metal batteries have the potential to more than double the specific energy of the state-of-the-art rechargeable Li-ion batteries, making Li-metal batteries a prime candidate for next-generation high-energy battery technology[1–3]. However, current Li-metal batteries suffer from fast cycle degradation compared with their Li-ion battery counterparts[2,3], preventing their practical adoption. A main contributor to capacity degradation is the disconnection of Li from the electrochemical circuit, forming isolated Li[4–8]. Calendar ageing studies have shown that resting in the charged state promotes further reaction of active Li with the surrounding electrolyte[9–12]. Here we discover that calendar ageing in the discharged state improves capacity retention through isolated Li recovery, which is in contrast with the well-known phenomenon of capacity degradation observed during the charged state calendar ageing. Inactive capacity recovery is verified through observation of Coulombic efficiency greater than 100% on both Li||Cu half-cells and anode-free cells using a hybrid continuous–resting cycling protocol and with titration gas chromatography. An operando optical setup further confirms excess isolated Li reactivation as the predominant contributor to the increased capacity recovery. These insights into a previously unknown pathway for capacity recovery through discharged state resting emphasize the marked impact of cycling strategies on Li-metal battery performance.

The accumulation of metallic Li that has become electronically isolated from the current collector (i-Li) is a pathway for substantial capacity loss in rechargeable Li-metal batteries (LMBs)[4–8]. Previous works have shown that this capacity loss is further exacerbated during charged state calendar ageing by enabling further reaction between Li and electrolyte[9–12]. These corrosion reactions generate additional by-products such as i-Li and solid electrolyte interphase (SEI), increasing interfacial impedance and contributing to further capacity loss.

To combat LMB capacity loss, recent studies have shown techniques to recover capacity in LMBs previously thought to be irreversible. Electrochemical strategies include applying high discharge current densities to promote dynamic spatial migration of i-Li towards reconnection with the electrode[8]. Chemical strategies include using iodine redox to free Li trapped in SEI and i-Li (ref. 13) and using polymer coatings to preferentially induce Li-ion reduction to Li metal to increase the probability of i-Li reconnection[14]. Furthermore, studies also suggest that a portion of the i-Li formed during intermittent charged state resting can be reconnected on the subsequent cycle. Although the average cycle performance of intermittently rested cells remains below that of continuously cycled cells, these results help emphasize that detrimental effects of corrosion can be lessened[10,15].

Discharged state capacity recovery

In this study, we ask if cycle performance can be further improved by resting LMBs in the discharged state in the absence of active Li corrosion. Calendar ageing anode-free electrodes in the discharged state and the charged state exposes the electrolyte to two distinctive electrode environments during rest (Fig. 1a). In the discharged state, the electrolyte interacts with only i-Li and residual SEI shells from previous cycles (r-SEI) during rest. In the charged state, the active Li remains connected to the electrode and can react with the electrolyte during rest, decreasing active Li capacity and generating excess SEI and i-Li. Although the detrimental effects of charged state calendar ageing have become well studied[9–12], the effects of discharged state calendar ageing are not well known.

To gauge the effect of discharged state calendar ageing on cycle performance, we compared the Coulombic efficiencies (CEs) of Li||Cu half-cells with localized high-concentration electrolyte (LHCE)[16] cycled using three different protocols: (1) 12-h rest at open circuit voltage (OCV) in the discharged state, (2) continuous cycling and (3) 12-h rest at OCV in the charged state (Fig. 1b). Counter to the performance degradation seen in cells rested in the charged state, we observe increased cycle performance in cells rested in the discharged state compared with

[1]Department of Materials Science and Engineering, Stanford University, Stanford, CA, USA. [2]Department of Chemistry, Stanford University, Stanford, CA, USA. [3]Department of Chemical Engineering, Stanford University, Stanford, CA, USA. [4]Stanford Institute for Materials Energy and Energy Sciences, SLAC National Laboratory, Menlo Park, CA, USA. [5]These authors contributed equally: Wenbo Zhang, Philaphon Sayavong. ✉e-mail: yicui@stanford.edu

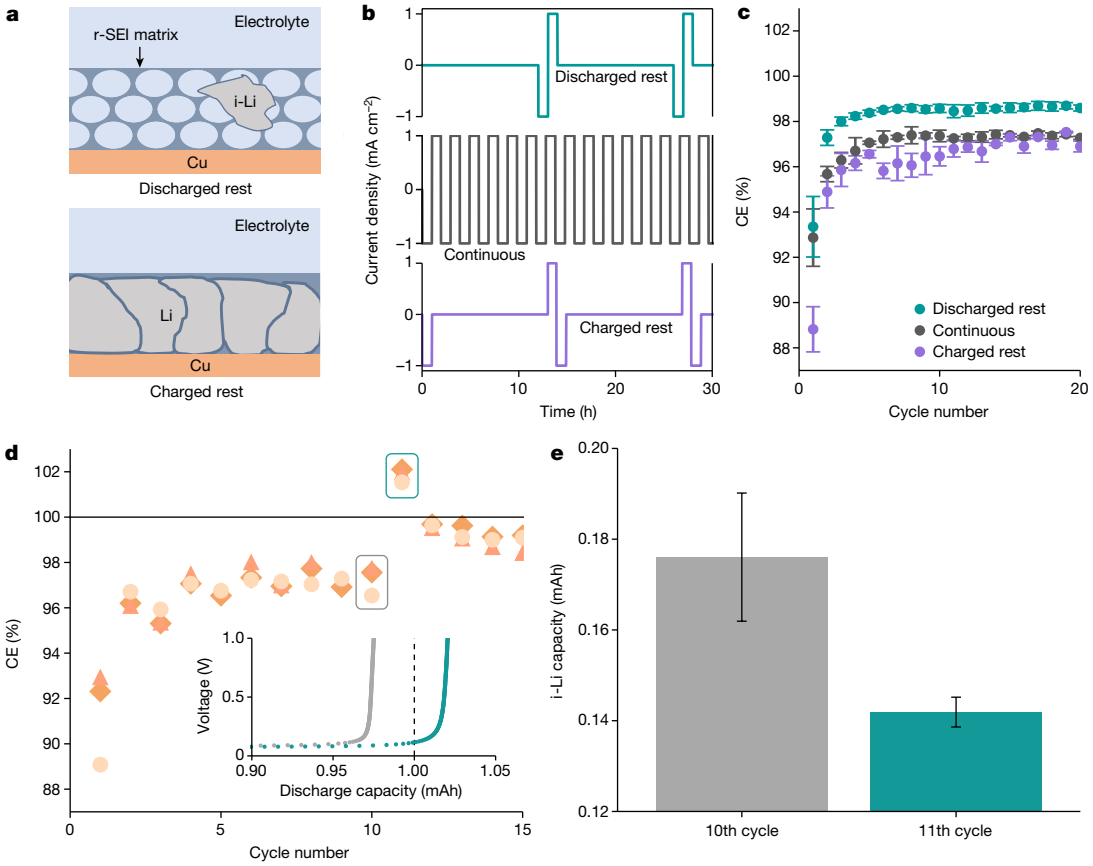

Fig. 1 | Capacity recovery from discharged state rest illustrated by CE and TGC data. a, Schematic depicting the anode calendar aged in the discharged state (top) and charged state (bottom). **b**, Current profiles. **c**, CE of Li||Cu half-cells running on cycling protocols with discharged state rest, no rest (continuous) and charged state rest. **d**, CE of Li||Cu half-cells running on the hybrid cycling protocol (10 continuous cycles followed by discharged rest for subsequent cycles). The 4.5% increase in CE between the 10th and 11th cycles shows greater than 100% CE in all three cells and demonstrates inactive capacity recovery. Inset, voltage profiles of the 10th (grey) and 11th (green) cycles. **e**, Capacity lost as i-Li on the current collectors at the end of the 10th and 11th cycles extracted from the TGC data. Error bars in **c** and **e** represent s.d.

continuously cycled cells. The discharged state rested cells show an average CE of 98.2% compared with the average CE of 96.9% for continuously cycled cells and 96.2% for charged state rested cells (Fig. 1c). The CE increase seen in discharged state rested cells suggests that resting in the absence of active Li corrosion enables additional capacity recovery.

The increase in cycle performance observed after discharged state resting can stem either from more efficient stripping of newly plated Li or from reactivation of i-Li from previous cycles. An effective method to demonstrate capacity recovery from previous cycles is to discharge more capacity than was charged, generating CEs greater than 100%. To conduct this test, we created a hybrid protocol that contains 10 continuous cycles followed by five cycles with 12-h rest in the discharged state (Extended Data Fig. 1a). During the initial 10 continuous cycles, lost capacity contributes to the build-up of i-Li and r-SEI. If resting in the discharged state aids in recovering capacity trapped in r-SEI and/or i-Li, a higher CE is expected in the first rested cycle compared with the continuous cycles. The three Li||Cu cells cycled on the hybrid protocol show an average 4.5% increase in CE (ΔCE) to greater than 101% on the 11th cycle, confirming that resting enables recovery of inactive capacity from previous cycles (Fig. 1d).

Further experiments conducted using various electrolytes (Extended Data Fig. 1b,c), charging capacities (Extended Data Fig. 2), discharge current densities (Extended Data Fig. 3), rest times (Extended Data Fig. 4) and number of continuous cycles (Extended Data Fig. 5) show similar capacity recoverability. These experiments help demonstrate that post-discharged rest capacity recovery is a generalizable phenomenon under a wide range of cycling conditions. An important result is the greater than 100% CE observed after a low discharge current density of 0.25 mA cm^{-2} post-discharged resting (Extended Data Fig. 3a). This result indicates that the discharged rest-induced capacity recovery and the high discharge current density capacity recovery found in a previous study[8] are two different recovery mechanisms.

Although the observation of greater than 100% CE on the hybrid protocol confirms excess capacity recovery from previous cycles, the CE data alone cannot determine whether the excess capacity originates from i-Li reactivation[17] or electrochemically reversible SEI reactivation[18]. To parse out the contribution of i-Li recovery, titration gas chromatography (TGC) is used to quantify the difference in i-Li capacity before and after discharged rest. The i-Li on the current collectors is reacted with water to form hydrogen gas in a 2:1 ratio according to the following chemical equation:

$$2Li\ (s) + 2H_2O\ (l) \rightarrow 2LiOH\ (aq) + H_2\ (g) \quad (1)$$

H_2 can also be formed through the reaction of H_2O with LiH ($LiH + H^+ \rightarrow Li^+ + H_2$). However, previous studies substituting D_2O for H_2O to parse out LiH and Li contributions have shown that LiH corresponds to <10% of the overall inactive Li capacity[4,19]. Therefore, most of the H_2 generated can be attributed to the capacity lost as i-Li. The results show that the continuous protocol cells have an average cumulative capacity loss of 0.175 mAh, whereas the hybrid protocol cells had a lower average cumulative capacity loss of 0.140 mAh (Fig. 1e). The lower

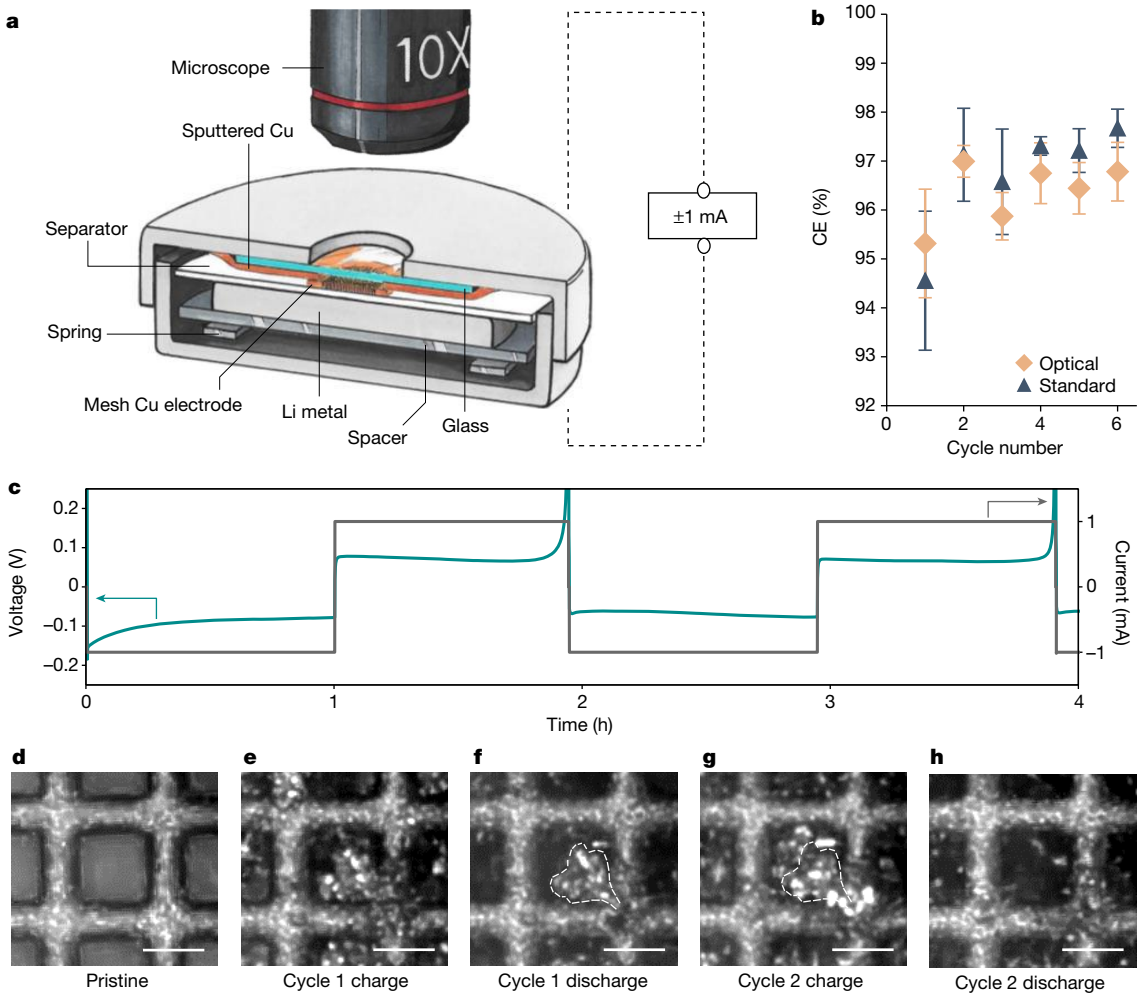

Fig. 2 | Operando optical microscopy of Li isolation and reconnection under continuous cycling. a, Cross-sectional schematic of the optical cell setup. **b**, CE of standard Li||Cu half-cells and optical Li||Cu half-cells for the first six cycles. Error bars represent s.d. **c**, Voltage and current profiles of the optical cell for the first two cycles. **d**–**h**, Optical images of the Cu mesh and separator taken in the pristine state (**d**), first-cycle charged state showing the formation of an Li deposit (**e**), first-cycle discharged state depicting the i-Li deposit outlined in white (**f**), second-cycle charged state showing new Li deposits plating on the previously i-Li deposit, demonstrating electrical reconnection (**g**), and second-cycle discharged state with the previously isolated deposit of Li recovered (**h**). Scale bar, 25 µm (**d**–**h**).

capacity loss (higher reversible capacity) on the 11th cycle compared with the 10th cycle is indicative of excess i-Li being recovered from the current collector after the rested cycle. Although SEI generation is the dominant pathway for capacity loss in high-performance electrolytes such as high-concentration electrolyte[19], the loss of 0.175 mAh to i-Li formation over 10 cycles demonstrates the significance of capacity lost to Li disconnection and the importance of minimizing and reactivating i-Li even for high-performing electrolytes.

Operando optical cell setup

In addition to demonstrating the efficacy of discharge rest on enhancing i-Li recovery, we also developed a pressurized operando setup (Fig. 2a) to enable a better understanding of the i-Li recovery mechanism. Many past optical platforms have shown important properties of Li metal plating and stripping without the use of stack pressure[20–22]. However, because this optical setup must closely replicate the CE and capacity recovery of a high-performing Li||Cu coin cell, stack pressure is an essential criterion that must be satisfied[23–25]. This is substantiated by the 15% decrease in CE observed in cells without stack pressure compared with those with stack pressure (Extended Data Fig. 6g). To mitigate the impact of cell form factor on cycle performance, the operando optical setup is fabricated from a standard coin cell to maintain stack pressure, enabling both microscope compatibility (Extended Data Fig. 6a–d) and high CE (Fig. 2b).

The optical time-lapse data corresponding to the voltage and current profiles in Fig. 2c show that i-Li can be recovered even during continuous cycling (Fig. 2d–h and Supplementary Video 1). Before cycling, the pristine Cu mesh on top of the separator can be seen (Fig. 2d and Extended Data Fig. 6e). During the first-cycle charging, Li is seen nucleating and growing from the bottom right corner of the Cu mesh (Fig. 2e). At the end of the first discharge cycle, a large i-Li deposit (white outline) is formed because of the electronic disconnection between the Li deposit and Cu electrode (Fig. 2f). During the second-cycle charging, fresh Li is seen depositing in the Cu mesh window. This is followed by new Li growth sprouting from the previously i-Li deposit, indicating electrical reconnection of the i-Li deposit with the electrode (Fig. 2g). After re-establishing electrical contact, the previously i-Li deposit is almost completely stripped away by the end of the second-cycle discharge, demonstrating i-Li recovery during continuous cycling (Fig. 2h).

To visualize the increase in i-Li recovery after calendar ageing in the discharged state, we mapped the area of i-Li and recovered i-Li (r-Li) in operando optical cells cycled with and without discharged state calendar ageing. Cell 1 (Fig. 3a–c and Supplementary Video 2) is cycled

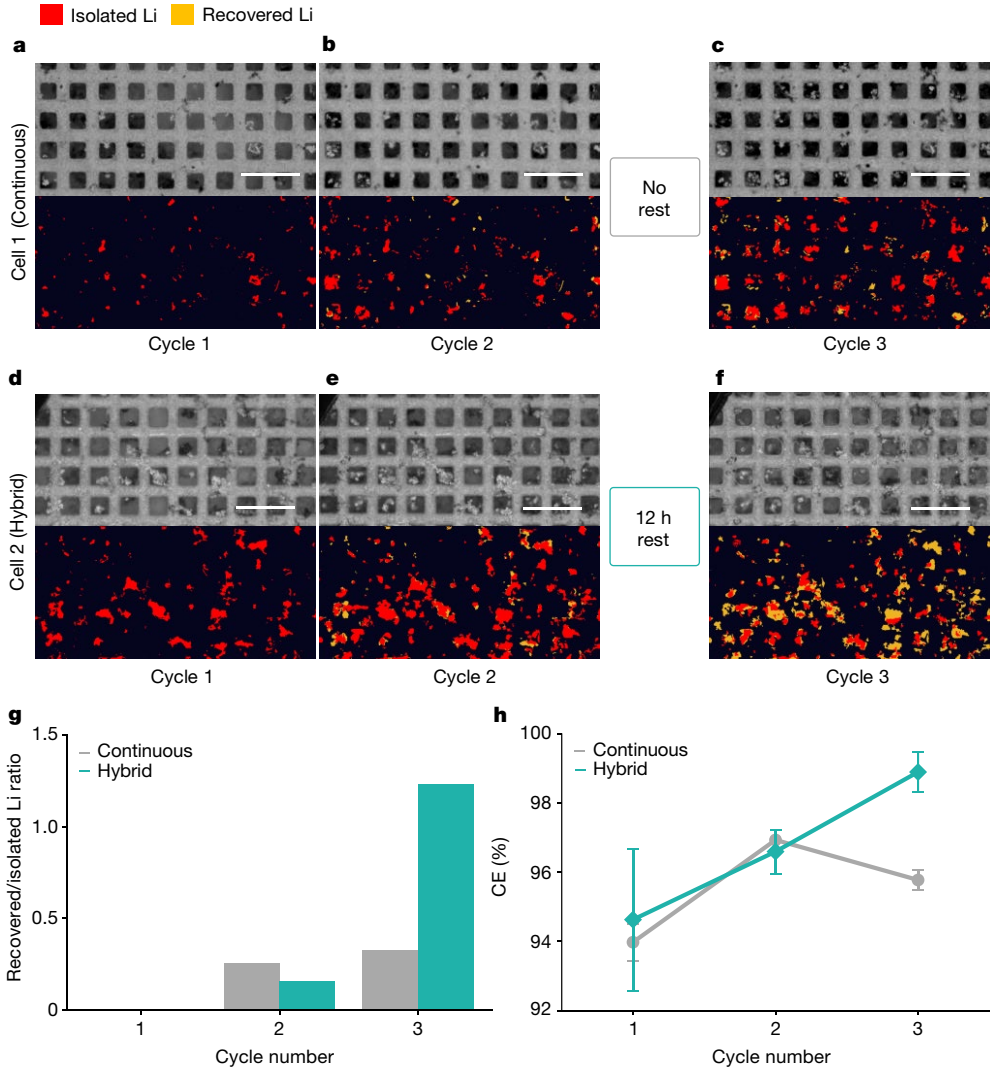

Fig. 3 | i-Li areal comparison between rested and continuously cycled optical cells. a–**c**, Cell 1, continuous cycling protocol: optical images (top) of Cu mesh in the discharged state for each respective cycle and colourmap (bottom) showing the area of i-Li (red) and r-Li (yellow) at the end of the first (**a**), second (**b**) and third (**c**) cycles. **d**–**f**, Cell 2, hybrid rest cycling protocol with 12-h discharged rest between the second and third cycles: optical images (top) of Cu mesh in the discharged state for each respective cycle and colourmap (bottom) showing the area of i-Li (red) and r-Li (yellow) at the end of the first (**d**), second (**e**) and third (**f**) cycles. Scale bar, 100 µm (**a**–**f**). **g**, *R*/*I* from the first to third cycles for both continuous and hybrid cells. **h**, CEs corresponding to the continuous and hybrid cycle cells. Error bars represent s.d.

continuously, and cell 2 (Fig. 3d–f and Supplementary Videos 3–5) is cycled on the hybrid resting protocol with two continuous cycles followed by 12 h of discharge rest and a third cycle. By comparing the respective r-Li to i-Li areal ratios (*R*/*I*), the optical data can be used to corroborate the increase in Li recovery observed in electrochemical data after discharged calendar ageing.

For the first cycle of cell 1, only newly formed i-Li is observed on the colourmap because there is no i-Li to recover from previous cycles (Fig. 3a). On the second and third cycles of cell 1 (Fig. 3b, c), both i-Li and r-Li are observed. However, the total area of i-Li generated greatly exceeds the area of r-Li during continuous cycling with respective *R*/*I* of 0, 0.25 and 0.33 for cycles 1, 2 and 3, respectively (Fig. 3g). Similar $R/I < 1$ is observed in cell 2 as cell 1 during the first ($R/I = 0$) and second cycles ($R/I = 0.16$) because their cycling protocols are the same up to the end of the second cycle (Fig. 3d,e,g). After the second-cycle discharge, the cycling protocols of cell 1 and cell 2 diverge. Cell 1 continues to third-cycle charging, whereas cell 2 is aged for 12 h before its third-cycle charging. As a result of the discharged state calendar ageing of cell 2, a considerable increase in the r-Li area and a decrease in the overall i-Li area is observed (Fig. 3f) resulting in an *R*/*I* of 1.23. This $R/I > 1$ corresponds to a greater area of i-Li being recovered than being generated, suggesting a net capacity recovery for the cycle. This increase in capacity recovery is also supported in the CE data that shows the cycle 3 CE of cell 2 at 98.9% and the cycle 3 CE of cell 1 at 95.8% (Fig. 3h). Although the third cycle CE of cell 2 is less than 100%, extensive i-Li recovery is still observed. This discrepancy can be attributed to some CE loss due to SEI production in earlier cycles. Studies have shown that 2–5% of capacity is lost to SEI formation during the first few cycles[4,19]; this leaves a best-case scenario of 98% of charging capacity dedicated to Li plating. In a cell with only 0.98 mAh of reversible capacity plated, a third-cycle CE of 98.9% would indicate the net recovery of 9 µAh of excess capacity. Moreover, an optical cell with a post rest discharge current density of 0.67 mA cm^{-2} achieved a comparable CE of 99.3% and an $R/I > 1$ (Extended Data Fig. 7c).

Proposed Li recovery mechanism

To validate the applicability of discharge calendar ageing in real LMBs, three $LiFePO_4$||Cu anode-free cells are cycled using a hybrid protocol

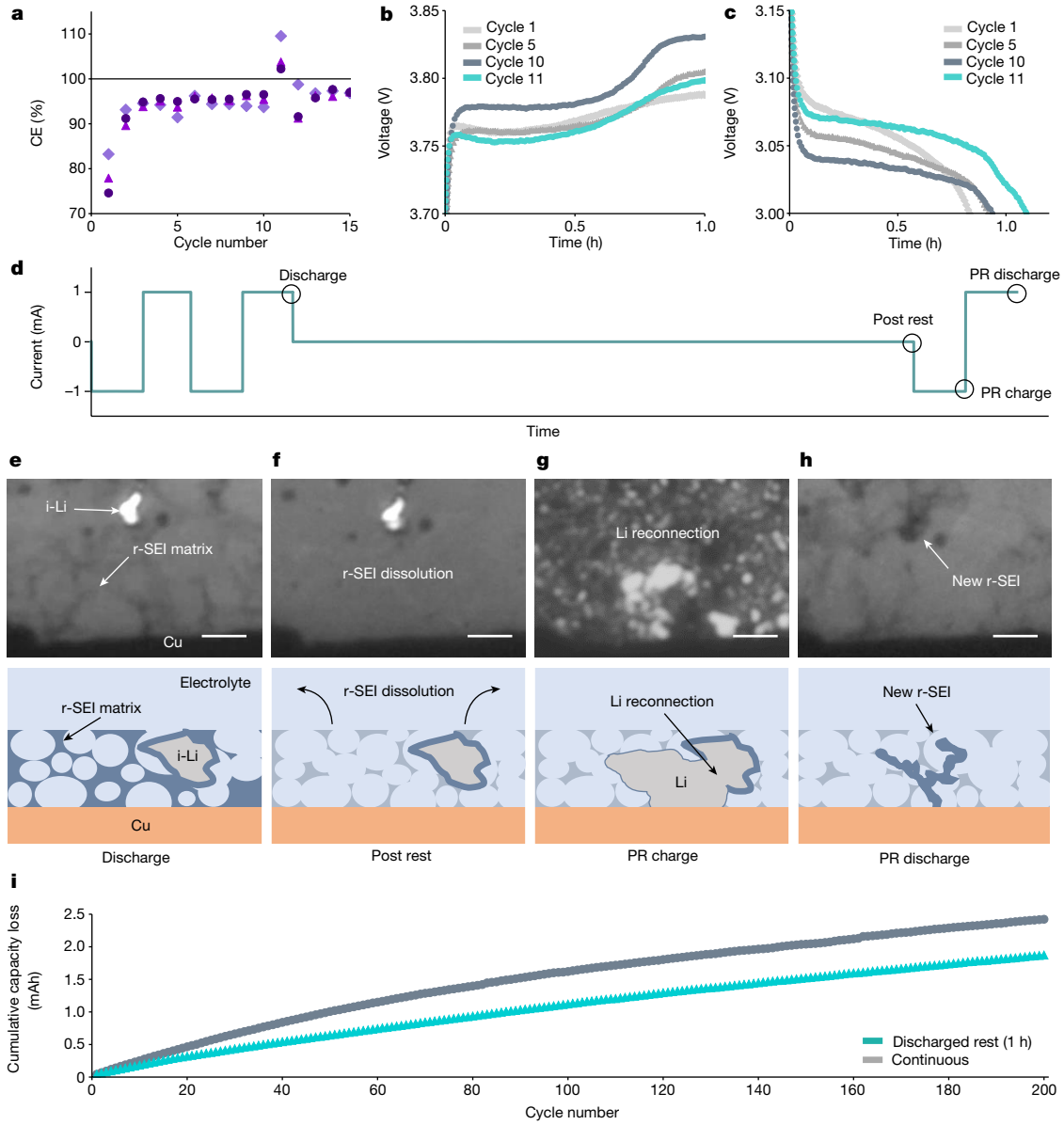

Fig. 4 | Rest-induced SEI dissolution and overpotential reduction. a, CE of $LiFePO_4$ anode-free coin cells running on a modified hybrid cycle with rest between the 10th and 11th cycles. **b**,**c**, Charging voltage (V_p) (**b**) and discharging voltage (V_s) (**c**) profiles of anode-free cells running on the modified hybrid cycling protocol for cycles 1, 5, 10 and 11. **d**, Cycle protocol for resting at discharge with time markers associated with the schematics below. **e**–**h**, Optical image and schematic of the proposed pathway for r-SEI dissolution and i-Li recovery. **e**, Discharge: Li can be isolated by thickening of r-SEI and by gas cavities formed during reduction. **f**, Post rest (PR): the electrolyte can dissolve r-SEI. **g**, PR charge: newly plated Li can reconnect and reactivate the previously i-Li. **h**, PR discharge: reconnected Li is stripped away until it can no longer maintain contact with the electrolyte or the current collector. New r-SEI is formed with some potential residual i-Li leftover. Scale bar, 5 µm (**e**–**h**). **i**, Cumulative capacity loss of Li||Cu half-cells running on 1-h discharged rest and continuous cycling protocols.

tailored for full cells. After 10 continuous cycles and a 12-h discharged rest period, the 11th cycle CE increases to greater than 100% (Fig. 4a). This result is consistent with the 11th cycle CE increase observed in Li||Cu half-cells (Fig. 1d), indicating that the benefits of discharged state resting are applicable to anode-free full cells. Further testing conducted on 200 mAh $LiFePO_4$||Cu anode-free pouch cells also shows greater than 100% CE post-discharged rest, demonstrating efficacy in high-capacity batteries (Extended Data Fig. 8a,b). The discharge resting protocol may also be relevant for full cells with excess Li. Once the active excess Li is consumed during cycling leaving behind i-Li and SEI, discharge rest can potentially enable recovery of some i-Li capacity to prolong cycle life. However, the investigation of discharge resting in different cell formats is left as a subject of future studies.

During constant current (I) cycling between the first and 10th cycles, the charging voltage V_p increases, whereas the discharge voltage V_s decreases. The difference between V_p and V_s (ΔV) increases by approximately 50 mV from the first cycle to the 10th cycle (Fig. 4b,c). This increase in overpotential observed during cycling has been correlated with the build-up of both i-Li and r-SEI impeding mass transport[7,9,26,27]. However, after discharged state resting, a 50-mV drop in ΔV is observed between the 10th and 11th cycles (Fig. 4b,c) suggesting a decrease in internal resistance that could be correlated with r-SEI dissolution. To test this hypothesis, the optical cell is set up to capture changes within the electrode during discharged state resting (Fig. 4d–h and Supplementary Video 6). At the end of the discharge cycle, the optical image shows a dark porous matrix with i-Li suspended in the middle

(Fig. 4e). This porous matrix conforms to the shape of the previously stripped Li that indicates this material is r-SEI that has been left behind; previous cryo-electron microscopy studies have also reported similar r-SEI morphologies[13,28]. During discharged state calendar ageing, the dark contrast of r-SEI is seen fading away, suggesting r-SEI dissolution into the electrolyte (Fig. 4f). Because r-SEI dissolution decreases the quantity of electronically insulating matrix surrounding i-Li, it increases the available surfaces on i-Li for reconnection during the charging cycle (Fig. 4g). The previously i-Li is thus activated and can be stripped away, increasing the CE and recovered capacity. A new r-SEI husk is left in its place (Fig. 4h).

Additional electrochemical and chemical experiments support the observation of r-SEI dissolution during resting at OCV. Data collected by electrochemical quartz crystal microbalance show notable SEI mass loss during resting at OCV for multiple electrolyte chemistries (Extended Data Fig. 9a). SEI dissolution is further supported by tests showing electrodes with preformed SEI require increased capacity to 'repair' the SEI when electrodes are rested at OCV for longer periods (Extended Data Fig. 9b). Furthermore, data from X-ray photoelectron spectroscopy characterization and NMR spectroscopy results show that r-SEI becomes more inorganic while electrolyte accumulates additional organic moieties after resting. This strongly suggests that organic components in the SEI are more prone to dissolution compared with the inorganic components (Extended Data Fig. 10a,b).

r-SEI dissolution and chemical corrosion of the i-Li are competing processes that occur simultaneously during discharged resting at OCV. Although r-SEI dissolution during discharged calendar ageing can help promote the reconnection of i-Li on the subsequent charging cycle, the corrosion reactions during rest can both reduce i-Li available for recovery and thicken the native SEI on i-Li. These factors can reduce the efficacy of Li reconnection[15,19,20]. Although our tests show that corrosion slightly reduces the efficacy of capacity recovery after 24 h of rest, all cells rested in the discharged state, regardless of rest period, demonstrate a significant increase in CE compared with the continuous cycles (Extended Data Fig. 4). This finding indicates that i-Li recovery, not i-Li corrosion, is the dominant factor affecting the cycle performance after discharged state rest. This result also aligns with previous Li corrosion studies that conclude capacity lost during 24-h charged state resting makes up less than 20% of total Li capacity. In the case of discharged resting, this implies more than 80% of i-Li should remain recoverable after 24 h of rest.

The solubility of r-SEI in the electrolyte has been reported to be limited[29]. As a result, prolonged cycling can eventually saturate the electrolyte with soluble r-SEI species, decreasing the efficacy of the discharged rest capacity recovery. The effects of prolonged cycling are tested by comparing the CE (Extended Data Fig. 8c) and cumulative capacity loss (Fig. 4i) of Li||Cu half-cells cycled with and without discharged rest over 200 cycles. In the first 100 cycles, the continuously cycled cells lose 44% more capacity than the discharge rested cells with an average difference of 0.50 mAh. Between cycles 101 and 200, the difference in capacity loss increases by only 0.05–0.55 mAh. The saturation of the electrolyte with soluble r-SEI species during later cycles is probably a contributing factor to the diminishing recovery efficacy. Nevertheless, the substantial capacity recovered by discharged rest in the first 100 cycles has a considerable impact on overall capacity retention even during prolonged cycling.

The reactivation of i-Li is both an electrochemical and physical process that requires plated Li metal to break through the SEI and reconnect with the i-Li. Therefore, Li plating morphology, which affects the surface area and force applied on i-Li, can affect i-Li recoverability. This work introduces an extra physical process of r-SEI dissolution during discharged resting to promote increased i-Li reconnection and recovery. Components such as current collector[30] or coatings[14] can also be designed to alter Li morphology to increase the efficiency of i-Li recovery. The investigation of cell component modification for i-Li recovery is a potential avenue for future studies. However, even without cell component modifications, the discharged rest protocol can realize notable cycle performance gains. As the implementation of cycling protocols does not increase manufacturing costs, the barrier of integrating the discharged rest protocol in commercial LMBs can be lower than that of manufacturing and materials-based changes.

In this study, we show that recovery of i-Li is an ongoing process during cycling that can be enhanced through calendar ageing of cells in the discharged state. The phenomenon of i-Li recovery is supported by CE values greater than 100% and TGC data collected from cells running on a hybrid cycling protocol after discharged state resting. Furthermore, an optical operando technique corroborates the electrochemical and TGC data by exhibiting greater areas of Li recovery in rested cells compared with non-rested cells. The enhancement of i-Li recovery through discharged state calendar ageing emphasizes the importance of cycling protocol and their effects on LMB performance. Furthermore, these findings can help guide future studies on capacity recovery techniques and aid in the advancement of LMBs towards widespread adaptation.

Online content

Any methods, additional references, Nature Portfolio reporting summaries, source data, extended data, supplementary information, acknowledgements, peer review information; details of author contributions and competing interests; and statements of data and code availability are available at https://doi.org/10.1038/s41586-023-06992-8.

1. Xiao, J. et al. Understanding and applying Coulombic efficiency in lithium metal batteries. *Nat. Energy* **5**, 561–568 (2020).
2. Hobold, G. M. et al. Moving beyond 99.9% Coulombic efficiency for lithium anodes in liquid electrolytes. *Nat. Energy* **6**, 951–960 (2021).
3. Louli, A. J. et al. Diagnosing and correcting anode-free cell failure via electrolyte and morphological analysis. *Nat. Energy* **5**, 693–702 (2020).
4. Xiang, Y. et al. Quantitatively analyzing the failure processes of rechargeable Li metal batteries. *Sci. Adv.* **7**, eabj3423 (2021).
5. Geise, N. R., Kasse, R. M., Weker, J. N., Steinrück, H.-G. & Toney, M. F. Quantification of efficiency in lithium metal negative electrodes via operando X-ray diffraction. *Chem. Mater.* **33**, 7537–7545 (2021).
6. Liu, H. et al. Plating/stripping behavior of actual lithium metal anode. *Adv. Energy Mater.* **9**, 1902254 (2019).
7. Chen, K.-H. et al. Dead lithium: Mass transport effects on voltage, capacity, and failure of lithium metal anodes. *J. Mater. Chem. A* **5**, 11671–11681 (2017).
8. Liu, F. et al. Dynamic spatial progression of isolated lithium during battery operations. *Nature* **600**, 659–663 (2021).
9. Boyle, D. T. et al. Corrosion of lithium metal anodes during calendar ageing and its microscopic origins. *Nat. Energy* **6**, 487–494 (2021).
10. Merrill, L. C., Rosenberg, S. G., Jungjohann, K. L. & Harrison, K. L. Uncovering the relationship between aging and cycling on lithium metal battery self-discharge. *ACS Appl. Energy Mater.* **4**, 7589–7598 (2021).
11. Wood, S. M. et al. Predicting calendar aging in lithium metal secondary batteries: the impacts of solid electrolyte interphase composition and stability. *Adv. Energy Mater.* **8**, 1801427 (2018).
12. Lin, D. et al. Fast galvanic lithium corrosion involving a Kirkendall-type mechanism. *Nat. Chem.* **11**, 382–389 (2019).
13. Jin, C. et al. Rejuvenating dead lithium supply in lithium metal anodes by iodine redox. *Nat. Energy* **6**, 378–387 (2021).
14. Ma, C. et al. Chemically induced activity recovery of isolated lithium in anode-free lithium metal batteries. *Nano Lett.* **22**, 9268–9274 (2022).
15. Merrill, L. C. et al. Role of coatings as artificial solid electrolyte interphases on lithium metal self-discharge. *J. Phys. Chem. C* **126**, 17490–17501 (2022).
16. Ren, X. et al. Enabling high-voltage lithium-metal batteries under practical conditions. *Joule* **3**, 1662–1676 (2019).
17. Zheng, J. et al. Physical orphaning versus chemical instability: is dendritic electrodeposition of Li fatal? *ACS Energy Lett.* **4**, 1349–1355 (2019).
18. Zhuo, Z. et al. Breathing and oscillating growth of solid-electrolyte-interphase upon electrochemical cycling. *Chem. Commun.* **54**, 814–817 (2018).
19. Fang, C. et al. Quantifying inactive lithium in lithium metal batteries. *Nature* **572**, 511–515 (2019).
20. Sanchez, A. J. et al. Plan-view *Operando* video microscopy of Li metal anodes: identifying the coupled relationships among nucleation, morphology, and reversibility. *ACS Energy Lett.* **5**, 994–1004 (2020).
21. Bai, P., Li, J., Brushett, F. R. & Bazant, M. Z. Transition of lithium growth mechanisms in liquid electrolytes. *Energy Environ. Sci.* **9**, 3221–3229 (2016).
22. Chen, X. R., Yan, C., Ding, J. F., Peng, H. J. & Zhang, Q. New insights into "dead lithium" during stripping in lithium metal batteries. *J. Energy Chem.* **62**, 289–294 (2021).

23. Fang, C. et al. Pressure-tailored lithium deposition and dissolution in lithium metal batteries. *Nat. Energy* **6**, 987–994 (2021).
24. Wang, H. et al. Efficient lithium metal cycling over a wide range of pressures from an anion-derived solid-electrolyte interphase framework. *ACS Energy Lett.* **6**, 816–825 (2021).
25. Louli, A. J. et al. Exploring the impact of mechanical pressure on the performance of anode-free lithium metal cells. *J. Electrochem. Soc.* **166**, A1291–A1299 (2019).
26. Liu, L. & Zhu, M. Modeling of SEI layer growth and electrochemical impedance spectroscopy response using a thermal-electrochemical model of Li-ion batteries. *ECS Trans.* **61**, 43–61 (2014).
27. Lv, D. et al. Failure mechanism for fast-charged lithium metal batteries with liquid electrolytes. *Adv. Energy Mater.* **5**, 1400993 (2015).
28. Han, B. et al. Conformal three-dimensional interphase of Li metal anode revealed by low-dose cryoelectron microscopy. *Matter* **4**, 3741–3752 (2021).
29. Sayavong, P. et al. Dissolution of the solid electrolyte interphase and its effects on lithium metal anode cyclability. *J. Am. Chem. Soc.* **145**, 12342–12350 (2023).
30. Oyakhire, S. T. et al. Electrical resistance of the current collector controls lithium morphology. *Nat. Comm.* **13**, 3986 (2022).

Methods

Electrolyte preparation

Electrolytes were prepared and handled in an argon-filled glovebox with an O_2 concentration of <0.2 ppm and H_2O concentration of <0.01 ppm. Localized high-concentration electrolyte (LHCE) was prepared by combining lithium bis(fluorosulphonyl)imide (LiFSI), 1,1,2,2-tetrafluoroethyl-2,2,3,3-tetrafluoropropyl ether (TTE) and 1,2-dimethoxyethane (DME) solution in the molar ratio of 1:1.2:3.

Li||Cu half-cell

Electrochemical measurements used 2032-type coin cells with 60 µl of localized high-concentration electrolyte (LiFSI–1.2DME–3TTE). High-purity Li foil (750 µm, 99.9% (Alfa Aesar)) and Cu foil (Pred Materials) were used in all experiments unless otherwise noted. Both the Li and Cu foils were punched to 1 cm^2. Cu was rinsed with ethanol (Fisher) and acetone (Fisher) before transferring it to the Ar glovebox for coin-cell assembly to remove surface contaminants. A single layer of Celgard 2325 trilayer PE/PP/PE was used at the separator. Li was mechanically sheared with a polyethylene scraper to remove the surface oxide and improve the electrical connection to the stainless steel coin cell. Half-cells (optical and standard) were all charged at a current density of 1 mA cm^{-2} up to an areal capacity of 1 mAh and discharged at a current density of 1 mA cm^{-2} to a cutoff voltage of 1 V unless specified otherwise. Three standard (non-optical) coin cells were run per cycling condition on an Arbin battery cycler at 25 °C.

TGC

A total of eight specialized Li||Cu half-cells were assembled in the same manner as standard Li||Cu cells except with two 12-µm thick polyethylene separators in place of a single 25-µm separator. This was done to ensure the most consistent extraction of i-Li from both the copper foil current collector and the separator closest to the current collector. Four cells ran 10 continuous cycles, whereas the other four cells ran a hybrid protocol consisting of 10 continuous cycles followed by a 12-h rest in the discharged state and a final 11th cycle. After disassembly of the coin cell, the copper foil and the separator with i-Li were placed in an 18-ml glass vial and sealed by plastic–aluminium flip caps and rubber stoppers under an argon environment. Next, 1 ml of mill-Q water was added to the vial and allowed to react for 3 min. Then, 1 mL of the gas in a glass vial was extracted and transferred for hydrogen quantification. Hydrogen concentration was measured by a gas chromatography instrument (SRI 8610 C) equipped with a thermal conductivity detector and tandem columns (3″ HAYESEP-D, 6″ MS 5 A) running at 40 °C and a nitrogen carrier gas.

Operando optical cell assembly and microscopy

Two coin cell components were modified to make the optical cell: (1) the positive casing and (2) the current collector. A 2-mm hole was first punched into the positive cap. A microscope cover glass was epoxied over the hole to ensure an airtight viewing window. A 1.5-mm wide strip of Kapton tape was placed on the glass to mask the middle of the 2-mm viewing window hole and 200 nm of copper was sputtered on the inside of the positive casing and glass. After the sputtering step, the Kapton tape mask was removed to reveal a strip of unsputtered area over the viewing window. A 3-mm 400 mesh copper TEM grid is placed in the middle of the viewing window hole such that the edges are in electrical contact with the sputtered copper (see Extended Data Fig. 6 for more information). The optical cells were imaged on an Olympus BX51 microscope at 10× magnification. A Swiftcam SC1803 camera was used to capture time-lapse images at an interval of 20 s.

Optical image to colourmap processing

The MP4 files collected on the optical microscope were converted to TIFF files before being imported into Imagej for further processing. Optical images used in Fig. 3 were selected to match with the times points at the end of the stripping step for cycles 1, 2 and 3. The raw RGB images from the microscope were split into three new images corresponding to the intensity of the red, green and blue in the raw images. The green channel image was selected for thresholding to separate the Li areas from the Cu areas because Cu lacked a green signal because of its reddish hue whereas Li was mostly reflected as whiteish light that did give off intensities in the green channel. A threshold was placed on the green channel image to separate the Li from the Cu mesh. However, owing to the non-uniform surface topography of the Cu mesh and Li, there are local areas of brightness that could not be filtered out with automated thresholding. To correct this, the researcher performed manual thresholding touch-ups to remove high-brightness areas in the Cu mesh to represent the areas of i-Li more accurately in the optical images.

First-cycle colourmaps depict the areas of i-Li left at the end of the first-cycle strip step in red. Second-cycle colourmaps depict new (formed second cycle) and remaining (formed first cycle) areas of i-Li in red. Areas previously occupied by i-Li formed in the first cycle that are recovered in the second cycle are depicted in yellow. Third-cycle colourmaps depict new (formed third cycle) and remaining (formed first and second cycles) areas of i-Li in red. Areas previously occupied by i-Li formed in the first and second cycles that are recovered in the third cycle are depicted in yellow.

Anode-free coin cell

Coin cells of 2032-type with a 1-cm^2 Cu foil anode (Pred Materials), 1 cm^2 $LiFePO_4$ (4 mAh cm^{-2} loading, MTI) and 60 µl of localized high-concentration electrolyte (LiFSI–1.2DME–3TTE) were used for cycling. The Cu was prepared and rinsed using the same procedure as those in the half-cell measurements. Once the coin cell was fabricated, two slow formation cycles (*C*/10, 0.4 mA cm^{-2}) were run, after which the cell was cycled at a moderate rate (*C*/4, 1 mA cm^{-2}), where *C* is the charging rate required to fully charge the battery in 1 h and *C*/10 denotes one-tenth of the *C* rate. Li is charged to a capacity of 1 mAh and discharged to a cutoff voltage of 3 V.

Anode-free pouch cell

Pouch cells with a loading of 200 mAh cm^{-2} were filled with 600 µl of localized high-concentration electrolyte (LiFSI–1.2DME–3TTE). The cells were cycled under this lean electrolyte conditions of 3 µl mAh^{-1} at a *C* rate of 1*C* (200 mA cm^{-2}). After assembly, the cells were rested for 48 h and clamped at 150 kPa before cycling. No formation cycles were run. The cells were charged to a voltage cutoff of 4 V and discharged to a cutoff voltage of 3 V.

XPS

X-ray photoelectron spectroscopy (XPS) was performed using the PHI Versaprobe IV instrument. The X-ray source was a monochromatic Al Kα source. The Li||Cu half-cells were disassembled in a glovebox. The Cu substrates were rinsed with 60 µl DME solvent before loading on the plate. The samples were transferred from the glovebox to the Versaprobe IV intro chamber using a vacuum transfer vessel to avoid any air exposure. The main chamber was maintained at approximately 10^{-7} Pa during any spectra collection. Electron and ion neutralizer guns were turned on before collecting the spectra. The sample height was maintained at 19.5 mm (maximum allowable *Z* height).

For XPS analysis, MultiPak software was used. C 1*s* peak at 284.5 eV was used as a reference for spectral shifting. The SEI atomic ratios were determined using the collected survey scans at 224 eV pass energy. The high-resolution signals were collected at 55 eV pass energy.

Electrochemical quartz crystal microbalance

Electrochemical quartz crystal microbalance measurements were performed using a QCM200 instrument (Stanford Research Systems), in which all the electrochemical testing was done in a glovebox filled

with argon with an O_2 concentration of less than 0.2 ppm and H_2O concentration of less than 0.01 ppm. Testing was done within the sensor holder itself, with a Li metal foil counter electrode. AT-cut quartz crystal coated with copper (Phillip Technologies) was used as the sensor and electrode for electrodeposition.

NMR

Small pieces of Li metal foil (roughly 1 × 1 × 1 mm size cubes) were soaked in 2 ml of electrolyte for 2 days. The electrolyte was then filtered through a 0.45-μm polytetrafluoroethylene filter. NMR measurements were performed on a Varian Mercury 400 MHz NMR. The temperature was set at 25 °C. The samples were prepared in the glovebox by injecting 300 μl of electrolyte into a new and dried NMR tube, together with 600 μl of newly opened methyl sulphoxide-d6 (Acros Organics, 99.9% D, max. 0.03% water impurity in each DMSO-d6 ampoules). It was then sealed with the PTFE caps and immediately put into the NMR machine for data acquisition. The samples were locked and shimmed using the external standard.

Data availability

All the data that support the findings of this study are available from the corresponding author upon request. Source data are provided with this paper.

Acknowledgements We acknowledge support from the Assistant Secretary for Energy Efficiency and Renewable Energy, Office of Vehicle Technologies of the US Department of Energy under the Battery Materials Research (BMR) Program and Battery 500 Consortium. D.T.B. acknowledges support from the National Science Foundation Graduate Research Fellowship Program. S.T.O. acknowledges support from the Knight Hennessy scholarship for graduate studies at Stanford University. R.A.V. acknowledges support from the National Academy of Sciences Ford Foundation Fellowship, the National Science Foundation Graduate Research Fellowship Program (NSF GRFP, grant no. DGE-1656518) and the Enhancing Diversity in Graduate Education (EDGE) Doctoral Fellowship Program at Stanford University. We also acknowledge T. Sogade for coin-cell material preparation. Part of this work was performed at the Stanford Nanofabrication Facility (SNF).

Author contributions W.Z., P.S. and Y.C. conceived the idea and created the cycling protocol. W.Z. designed the optical cell and performed the optical mapping analysis. X.X. performed TGC experiments. W.Z., D.L. and P.S. designed full cell experiments. W.Z. and P.S. analysed and interpreted the results. S.B.S. performed and analysed the XPS experiments. S.T.O., R.A.V., D.T.B., S.C.K., M.S.K., S.E.H., S.F.B. and Y.Y. assisted in result interpretation and feedback. D.L. assisted with figure creation. W.Z. and P.S. wrote the paper.

Competing interests The authors declare no competing interests.

Additional information
Supplementary information The online version contains supplementary material available at https://doi.org/10.1038/s41586-023-06992-8.
Correspondence and requests for materials should be addressed to Yi Cui.
Peer review information *Nature* thanks Chengbin Jin and the other, anonymous, reviewer(s) for their contribution to the peer review of this work. Peer reviewer reports are available.
Reprints and permissions information is available at http://www.nature.com/reprints.

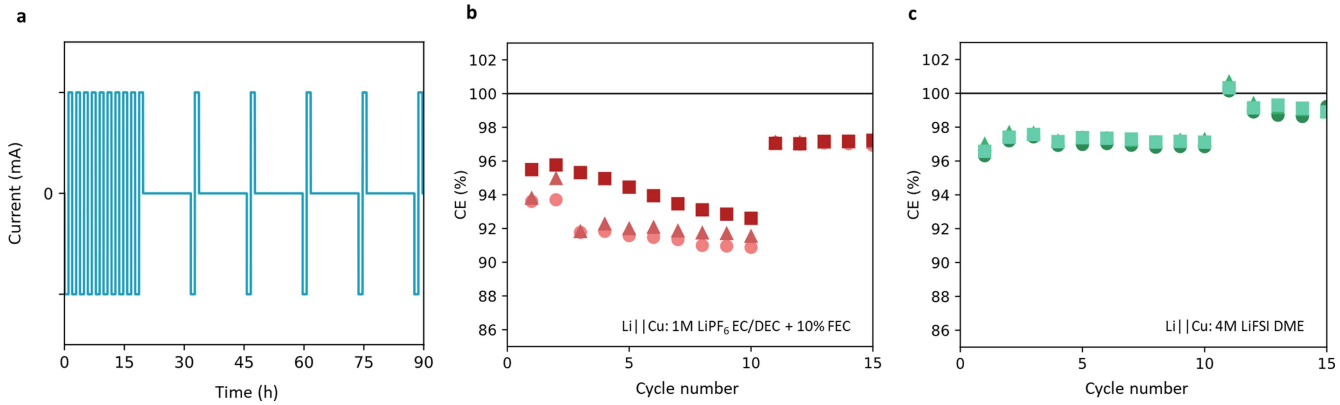

Extended Data Fig. 1 | Hybrid cycling protocol and corresponding CE. CE of Li||Cu half-cells running on the hybrid cycling protocol for **a**, Current profile of Li||Cu half-cell running the hybrid cycle protocol. The first 10 cycles are continuous. 11th cycle starts with a 12-hour rest period in the discharged state followed by 11th cycle charge and discharge. Discharged state rest is applied during every subsequent cycle. **b**, 1 M $LiPF_6$ with EC/DEC (ethylene carbonate/diethyl carbonate) + 10% FEC (fluoroethylene carbonate) and **c**, 4 M LiFSI DME (dimethoxyethane). Cells cycled with 1 M $LiPF_6$ EC/DEC + 10% FEC demonstrated an average ΔCE increase of greater than 5% between the 10th and 11th cycle. However, the 11th cycle CE does not exceed 100%. This may be due to the dendritic nature of Li morphology formed in carbonate electrolytes leading to faster corrosion, and increased native SEI formation on the i-Li. Nevertheless, the 11th cycle CE is greater than that of every prior continuous cycle, strongly suggesting capacity recovery is taking place. The cells cycled with 4 M LiFSI DME demonstrate greater than 100% CE for the 11th cycle with an average ΔCE increase of greater than 3% between the 10th and 11th cycle.

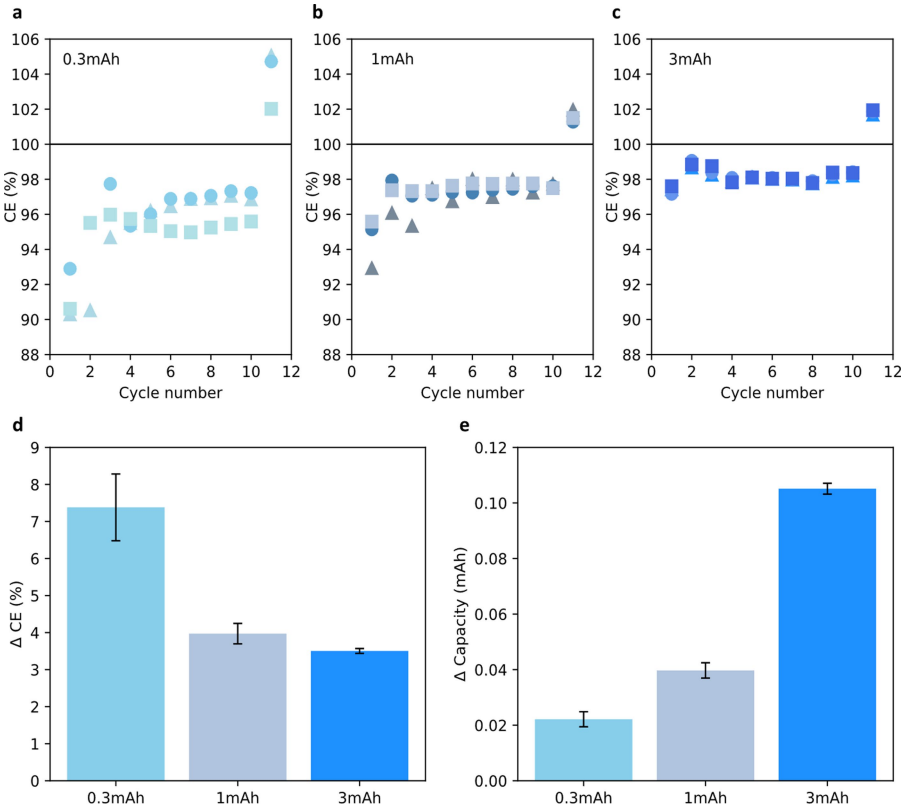

Extended Data Fig. 2 | Various charging capacity hybrid cycle performance. CE of Li | |Cu half-cells running with LHCE (LiFSI: 1.2 DME: 3 TTE) on the hybrid cycling protocol (10 continuous cycles followed by discharged rest for subsequent cycles) plated to capacities of **a**, 0.3mAh. **b**, 1mAh. **c**, 3mAh. The average CEs of the continuous cycles increase with increasing capacities, which can be attributed to lower surface area to volume ratio, and higher stack pressure. The post discharged rest ΔCE increase brings the 11th cycle CE to greater than 100% for all capacities cycled. **d**, the average ΔCE between the 10th and 11th cycle decreases with increase capacity due to more efficient cycling during the continuous cycles leading to a smaller fraction of active Li becoming isolated Li. The effect of lower average CE during continuous cycling leading to a higher ΔCE is most prominently demonstrated in cells cycled to a capacity of 0.3mAh. This is likely due to a higher percentage of plated capacity lost during the initial 10 cycles compared to cells cycled to 1mAh and 3mAh. The difference between the ΔCE of 1mAh and 3mAh are less significant. **e**, plot of Δ capacity (difference between 10th and 11th cycle discharged capacity) for all three capacity conditions after discharged state calendar ageing. Error bars in **d** and **e** represent s.d.

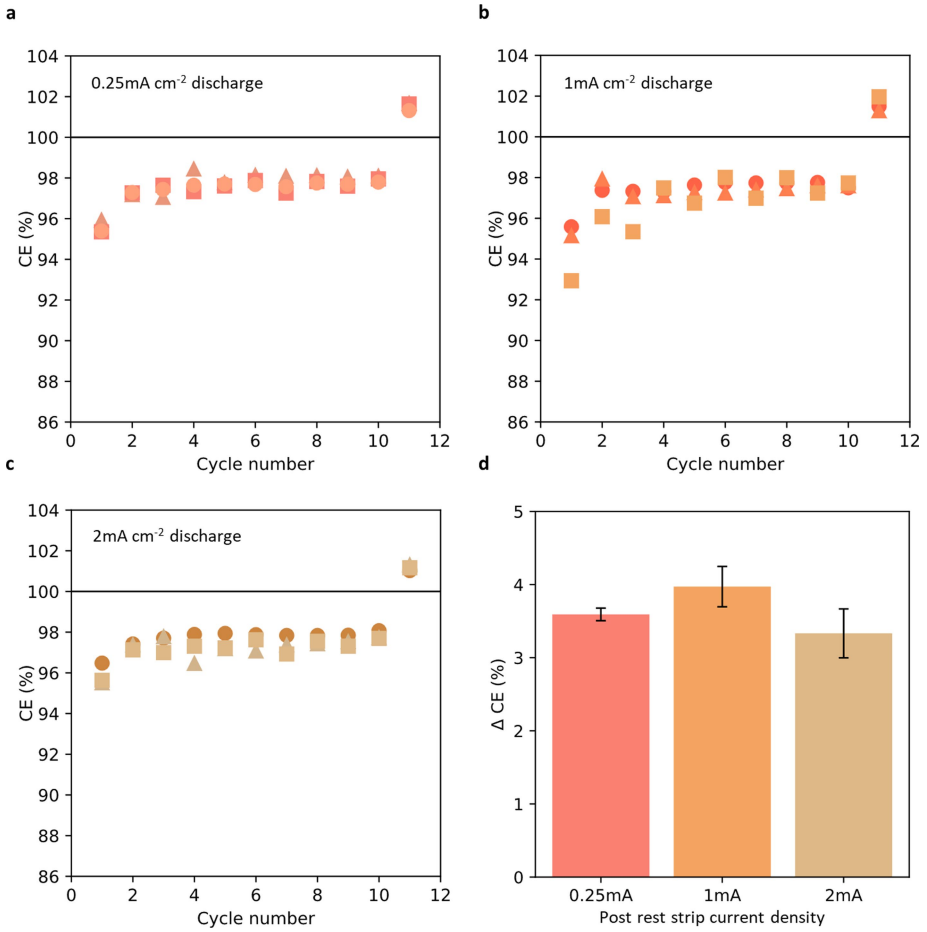

Extended Data Fig. 3 | Various discharge current density hybrid cycle performance. CE of Li||Cu half-cells running with LHCE on the hybrid cycling protocol (10 continuous cycles at 1 mA cm^{-2} and 1mAh followed by discharged rest for subsequent cycles) with various 11^{th} cycle discharge current densities of **a**, 0.25 mA cm^{-2}. **b**, 1 mA cm^{-2}. **c**, 2 mA cm^{-2}. **d**. Average ΔCE increase between the 10^{th} and 11^{th} cycle does not vary considerably from discharge current densities of 0.25 mA cm^{-2} to 2 mA cm^{-2}. This result indicates that quantity of capacity recovered after discharged calendar ageing has little dependence on the discharge current density. Error bars in **d** represent s.d.

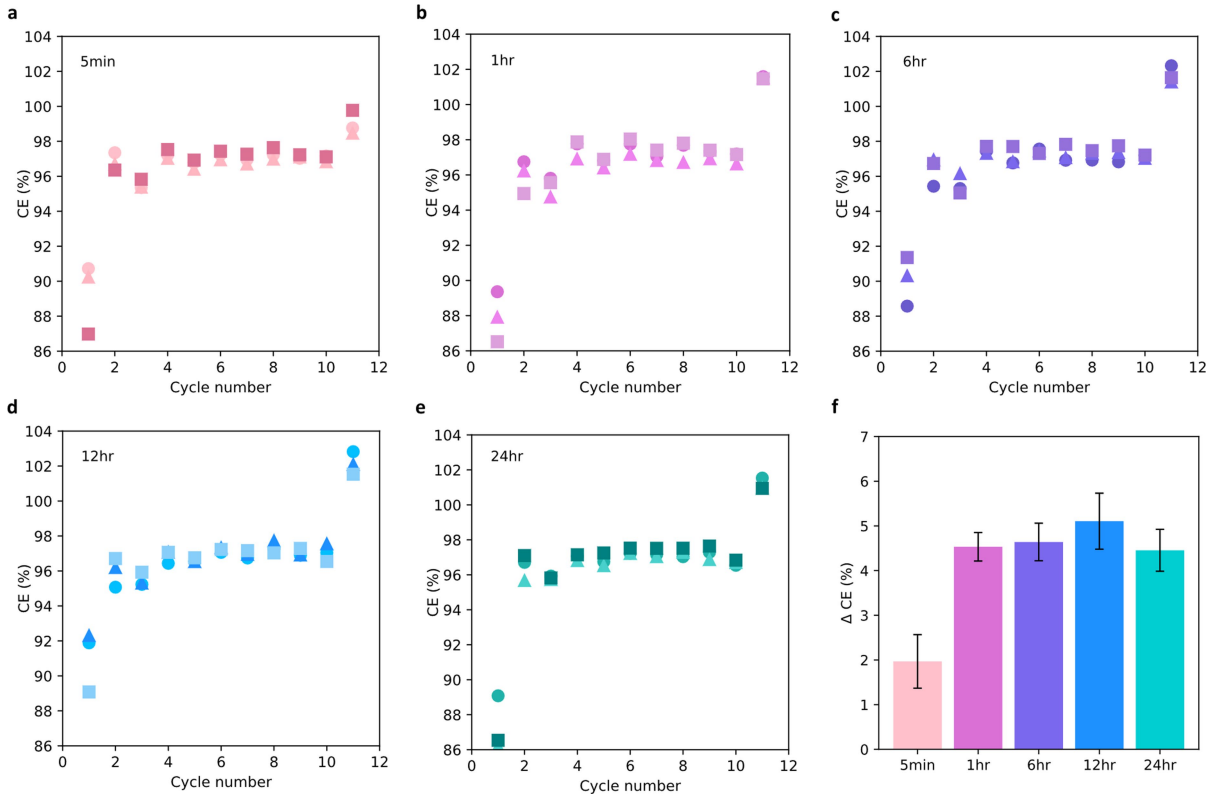

Extended Data Fig. 4 | Various rest time hybrid cycle performance. CE of Li | |Cu half-cells running with LHCE on the hybrid cycling protocol (10 continuous cycles followed by discharged rest for subsequent cycles) with various 11th cycle rest times of **a**, 5 min. **b**, 1 h. **c**, 6 h. **d**, 12 h. **e**, 24 h. **f**, Average ΔCE for all discharged state rests times between 5 min and 24 h. The increase in ΔCE from 5 min to 12 h suggests increased time for r-SEI dissolution and more favorable environment for reconnection. The decrease in ΔCE seen at 24 h of rest compared to at 12 h of rest can be driven by the larger role Li metal corrosion plays at longer rest times. Corrosion of isolated Li and dissolution of residual SEI both occur concurrently during discharged rest. The corrosion of isolated Li can reduce the quantity of metallic isolated Li available for recovery as well as thicken the native SEI on isolated Li. These factors can reduce the efficacy of Li reconnection, decreasing the ΔCE recovered for longer rest periods. However, the data for the 24 h discharged rests still shows 11th cycle CE greater than 100%. This strongly suggests that isolated Li recovery, not isolated Li corrosion, remains the dominant factor driving cycle performance, even after longer discharged state resting periods. Error bars in **f** represent s.d.

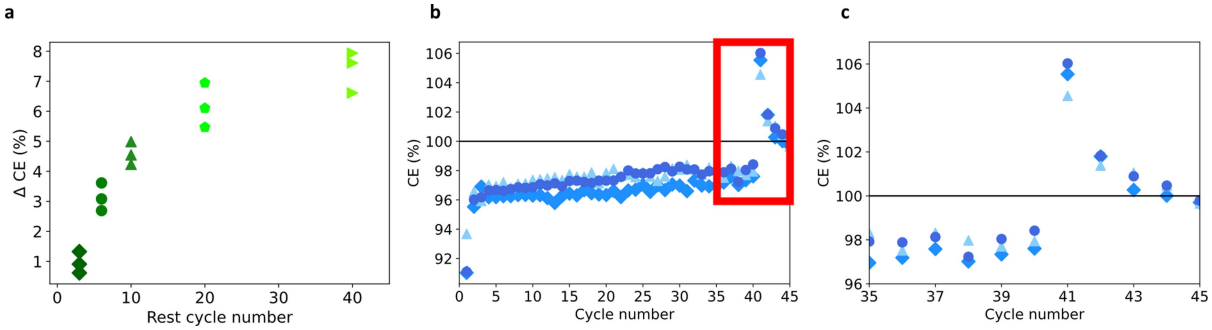

Extended Data Fig. 5 | Various rest cycle number hybrid cycle performance. **a**, The relationship between the rest cycle number and ΔCE (the CE difference on the last continuous cycle and the first rested cycle) is investigated. Tests were conducted varying the first discharge rest cycle from the 3rd to 40th cycle while keeping the 12-hour rest period constant. The results show that capacity recovery increases with cycle number, however, the data follows a power law trend rather than a linear trend. This is most likely due to SEI and isolated Li buildup limiting mass transport in later cycles, causing isolated Li from early cycles to become increasingly inaccessible for electrical reconnection. However, once the top layers of isolated Li are recovered after rest, there is less material impeding the recovery of prior layers of isolated Li in subsequent cycles, allowing for additional capacity recovery. **b**, This phenomenon is observed in the three cells which ran 40 continuous cycles hybrid protocol revealing greater than 100% CE in the four cycles following the start of resting. **c**, Zoomed in view of CE for cycle 35–45. All cells tested were cycled with LHCE.

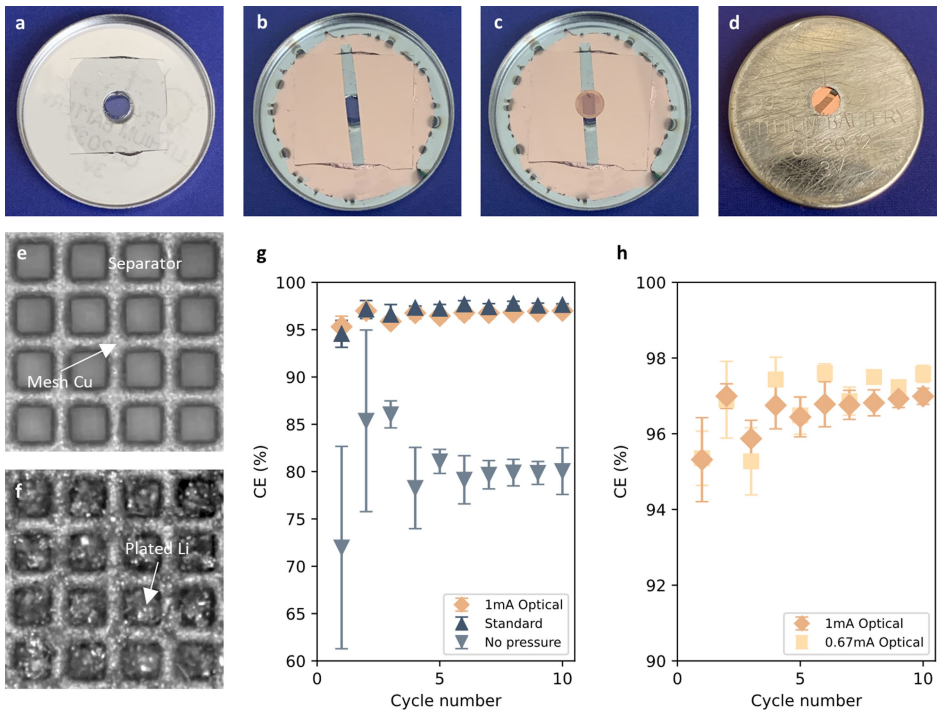

Extended Data Fig. 6 | Optical cell assembly and cycle performance. Images of the modified positive casing and current collector of the in-operando cell. **a**, shows the hole punched along with the glass window epoxied on. **b**, 200 nm of Cu is sputtered on with a 1.5 mm strip left un-sputtered across the window. **c**, a Cu mesh TEM grid is placed in the center of the window. **d**, assembled cell with the optical window facing up. Plan view though optical window of the Li | |Cu optical half-cell at the: **e**, pristine state prior to cycling, and **f**, with Li plated after first cycle plating at 1 mA cm^{-2} 1mAh. **g**, Comparison of the CE between optical cells, standard coin cells, and pressure-free coin cells. All cells were cycled at a current density of 1 mA cm^{-2} and a capacity of 1mAh with LHCE. The optical cell and the standard coin cell with similar stack pressure have comparable CEs. The "no pressure" coin cells are assembled with the Li metal counter and the Cu current collector separated by a gap of 2 mm. The average CE of the "no pressure" cells is 15% lower than that cells with stack pressure, emphasizing the large effect pressure has on cycle performance. **h**, Comparison of the CE between optical cells run at 1 mA cm^{-2} and 0.67 mA cm^{-2}. The Cu mesh has 2/3 the frontal surface area compared to bare Cu current collector, enabling local current densities of 1.5 mA cm^{-2}. on the Cu mesh grid when cycling at 1 mA. Reducing the current density from 1 mA to 0.67 mA normalizes the local current density on the Cu grid to 1 mA cm^{-2}. The similarities in CE of optical cells running at 1 mA and 0.67 mA demonstrates that variation between 1 mA cm^{-2} and 1.5 mA cm^{-2} does not greatly affect cycle performance. Error bars in **g** and **h** represent s.d.

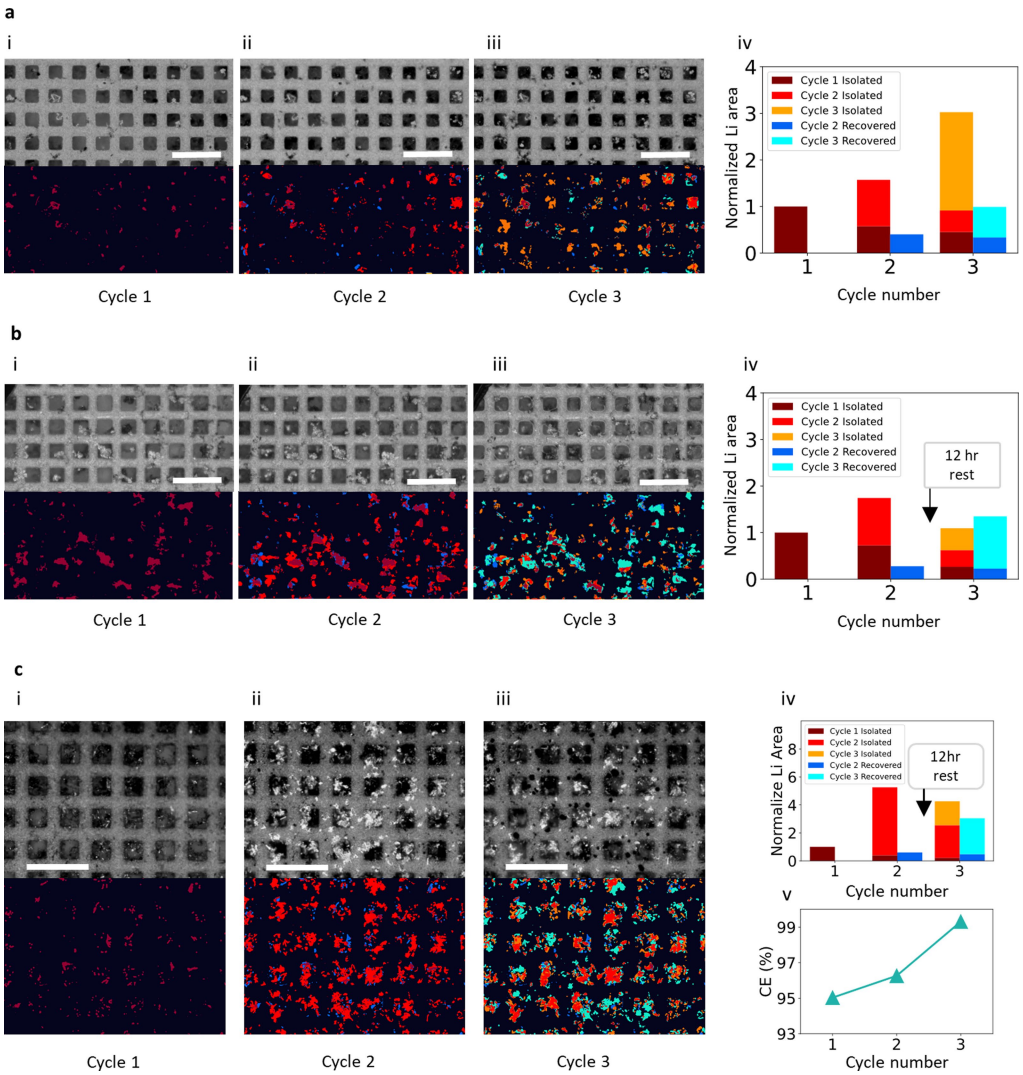

Extended Data Fig. 7 | Optical cell colored areal maps of isolated and recovered Li. Colored areal maps of i-Li and recovered Li (r-Li) for each cycle comparing cells cycled with and without discharged rest after cycle 2 at a capacity of 1mAh for all cycles. Maroon, red, and orange correspond to i-Li formed from cycle 1, 2 and 3 respectively. Blue and cyan correspond to recovered Li from cycles 2 and 3 respectively. **a**-**c** Optical images (top) and threshold colormaps (bottom) of i-Li and r-Li in each cycle of Cell-1 running the continuous cycling protocol and current density of 1 mA cm^{-2} (**a.i-a.iii**), Cell-2 running the hybrid cycling protocol and current density of 1 mA cm^{-2} (**b.i-b.iii**), Cell-3 running the hybrid cycling protocol and current density of 0.67 mA cm^{-2} (**ci-c.iii**). Plots of the areas occupied by i-Li and r-Li for Cell-1 (**a.iv**), Cell-2 (**b.iv**), and Cell-3 (**c.iv**). CE for Cell-3 (**c.iv**). The i-Li area is normalized to cycle 1 i-Li. Scale bar 100µm. The r-Li to i-Li ratio (R/I) is calculated by dividing the area of r-Li by the area of i-Li for that specific cycle. 2nd cycle R/I is calculated by dividing the blue area by the red area. 3rd cycle R/I is calculated by dividing the cyan area by the orange area. Since the areal map data cannot incorporate the volume and movement in Li deposits, the R/I ratio is an approximation for the quantity of r-Li and i-Li rather than the exact amount. However, the stack pressure and Cu mesh help to mitigate thickness variability and Li movement. In the instances i-Li deposits are displaced, the previously i-Li location is marked as "recovered" at the pre-displacement location and as "isolated" at a new location. The R/I for this Li deposit would be approx. 1 and therefore would not be counted toward i-Li or r-Li. Cells were cycled with LHCE.

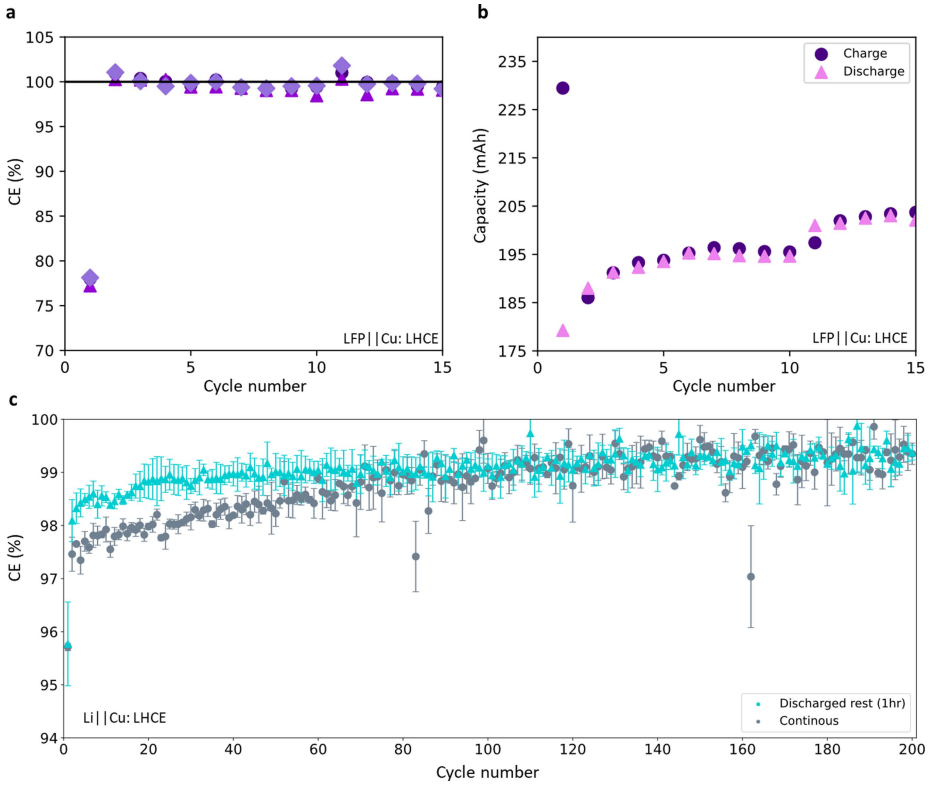

Extended Data Fig. 8 | LFP | |Cu pouch cell and long cycle Li | |Cu half-cells cycle performance. a, CE of $LiFePO_4$ (LFP) anode-free pouch cells running on a hybrid cycle with rest between the 10th and 11th cycle. The cells have a loading of approx. 200mAh and an electrolyte to capacity ratio of 3 µl mAh^{-1}. Cells were set to a pressure of 150 kPa and are charged and discharged at 1 C between 3 V and 4 V. No formation cycle is run so all the capacity lost and recovered during cycling is accounted for in the CE plot. The average 11th cycle post discharge rest CE is 101%, demonstrating that i-Li recovery though discharged state calendar ageing is viable in high capacity, lean electrolyte anode-free LMBs. **b**, charge and discharge capacity of the LFP anode-free pouch cell running on a hybrid cycle. A substantial increase in capacity of approx. 3.6mAh can be observed on the 11th cycle discharged which is maintained for the subsequent rested cycles. **c**, CE of Li | |Cu half-cells cycling with 1-hour discharged rest every cycle and continuous protocols. The beneficial effect of discharged rest is most apparent in the first 40 cycles where cells rested during discharged rest have an average CE 0.74% greater than continuously cycled cells. This CE gap between the two cycling conditions diminishes with increasing cycle numbers and converge around the 100th cycle. The saturation of the electrolyte with r-SEI species potentially decreases r-SEI dissolution and isolated Li recovery. This is likely a major driver of the decrease in CE gap. Cells cycled with LHCE. Error bars in **c** represent s.d.

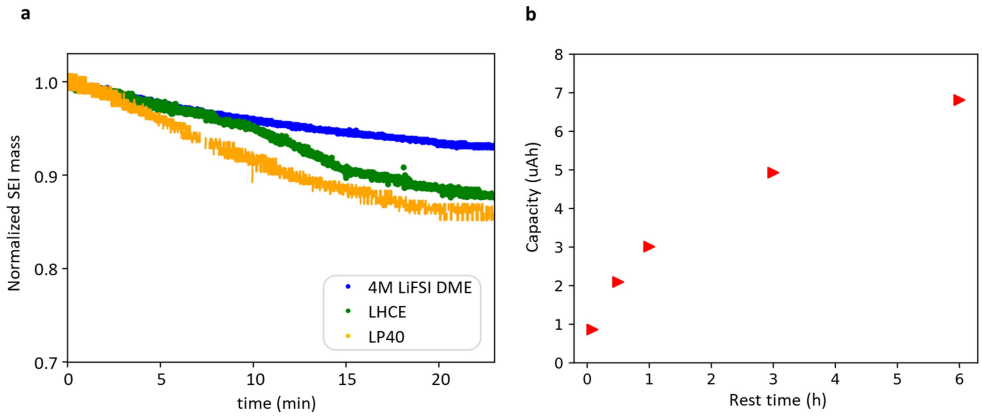

Extended Data Fig. 9 | SEI dissolution. a. SEI dissolution was quantified using electrochemical quartz crystal microbalance (EQCM). SEI is formed on the surface of the EQCM and then allowed to rest at open circuit voltage. This creates a similar environment to resting a cell in the discharged state. The results show a substantial drop in the normalized SEI mass during rest. 4 M LiFSI in DME is represented in blue, LHCE in green and LP40 in orange. Detailed experimental method can be found at https://pubs.acs.org/doi/10.1021/jacs.3c03195. Since organic SEI components are generally more soluble (Extended Data Fig. 10), we believe that electrolyte formulations have a considerable effect on how much i-Li is recovered. SEIs derived from anion-rich Li solvation structure have more insoluble and inorganic SEIs, likely decreasing Li recovery during discharged state rest. Electrolyte formulations also affect Li plating morphology, and likely also affect the probability of Li reconnection. Dendritic Li morphologies can have a lower likelihood of i-Li reconnection because of increased favorability of elastic deformation when a pressure is acted upon it. On the other hand, non-dendritic morphologies likely have higher probability of recovery due to increased favorability of plastic deformation under pressure, enabling reconnection. Reprinted (adapted) with permission from J. Am. Chem. Soc. 2023, 145, 22, 12342–12350. Copyright 2023 American Chemical Society. **b**, SEI degradation test: SEI was formed on the current collector of five Li | |Cu half-cells with LHCE. A constant current of −0.1 mA was applied until a voltage of 10 mV above plating potential followed by a constant voltage hold of 10 mV until the current of −0.5uA (CC-CV). The cells were then rested for different time periods (x-axis) before running a second CC-CV cycle identical to the first. The SEI degradation over rest can be related to the capacity (y-axis) used during the second CC-CV cycle.

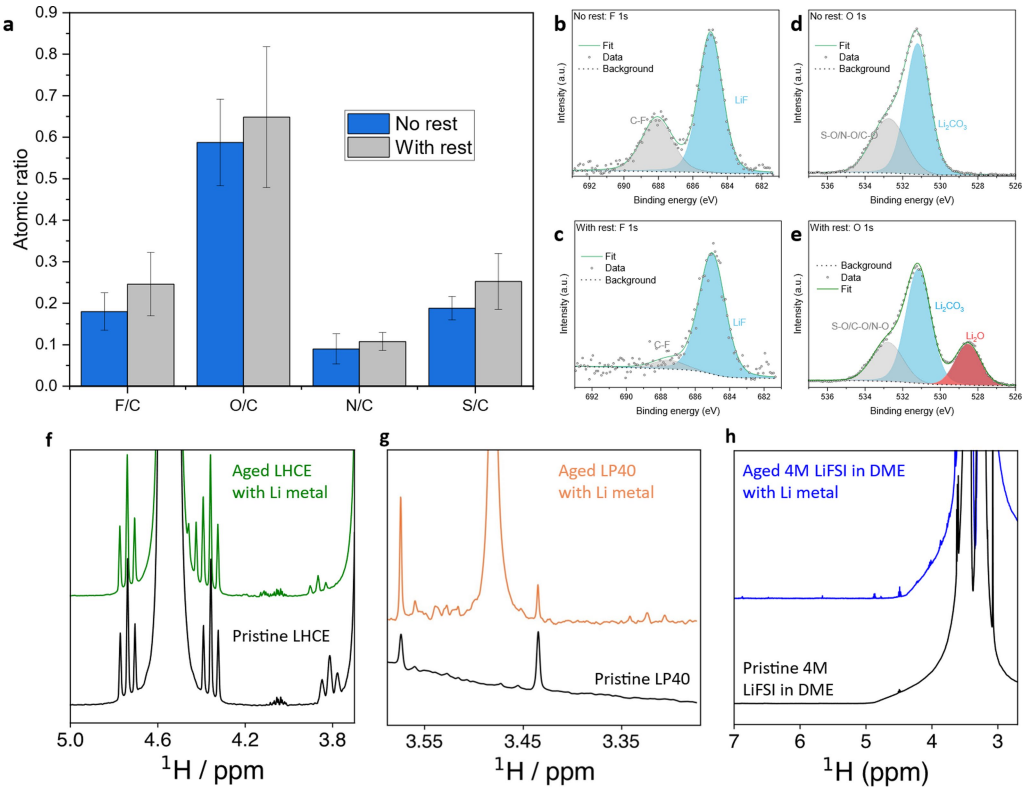

Extended Data Fig. 10 | NMR and XPS analysis of discharge rested SEI and electrolyte. a, XPS atomic ratios of the SEI on discharged Cu current collector of Li | |Cu cell with and without rest. The atomic ratio of F/C, O/C, N/C and S/C all increased after rest, suggesting the dissolution of SEI favors organic compounds. XPS spectra of Li | |Cu cells in the stripped state for F 1 s with no rest (**b**) and with rest (**c**) and O 1 s with no rest (**d**) and with rest (**e**). The increase in LiF to C-F signal ratio and the appearance of Li_2O after rest supports the notion of r-SEI dissolution favoring organics compounds over inorganic compounds. Two cells and six sample locations were run for each cycle condition. Cells were run for 1 complete cycle at a current density of 1 mA cm^{-2} and a capacity of 1mAh with LHCE. **f**, NMR analysis of pristine LHCE electrolyte and aged electrolyte in Li metal. Additional peaks can be seen in the in the aged electrolyte due to soluble organic SEI components. **g**, NMR analysis of pristine LP40 electrolyte and aged electrolyte in Li metal. Additional peaks can be seen in the in the aged electrolyte due to soluble organic SEI components. **h**, NMR analysis of pristine 4 M LiFSI in DME electrolyte and aged electrolyte in Li metal. Additional peaks can be seen in the in the aged electrolyte due to soluble organic SEI components. The chemical shifts of the additional species suggest that they are derived from solvents (carbonate-based for LP40 and ether-based for the rest) used in the electrolyte. However, full NMR characterization of SEI soluble species is not possible for our experimental setup, due to the low concentration of the SEI species. Error bars in **a** represent s.d. Reprinted (adapted) with permission from J. Am. Chem. Soc. 2023, 145, 22, 12342–12350. Copyright 2023 American Chemical Society.